

Emerging topological characterization in non-equilibrium states of quenched Kitaev chains

Y. B. Shi,¹ X. Z. Zhang,^{2,*} and Z. Song^{1,†}

¹*School of Physics, Nankai University, Tianjin 300071, China*

²*College of Physics and Materials Science, Tianjin Normal University, Tianjin 300387, China*

Topological characteristics of quantum systems are typically determined by the closing of a gap, while the dynamical quantum phase transition (DQPT) during quantum real-time evolution has emerged as a nonequilibrium analog to the quantum phase transition (QPT). In this paper, we illustrate that the system dynamics can be elucidated by considering the precession of a collection of free-pseudo spins under a magnetic field based on the exact results of extended Kitaev chains. The topology of the driven Hamiltonian is determined by the average winding number of the non-equilibrium state. Furthermore, we establish that the singularity of the DQPT arises from two perpendicular pseudo-spin vectors associated with the pre- and post-quenched Hamiltonians. Moreover, we investigate the distinct behaviors of the dynamic pairing order parameter in both topological and non-topological regions. These findings offer valuable insights into the non-equilibrium behavior of topological superconductors, contributing to the understanding of the resilience of topological properties in driven quantum systems.

Introduction.— Quantum theory provides a comprehensive framework for describing the equilibrium properties of quantum matter. However, earlier significant theoretical [1–6] and experimental progress [7, 8] has greatly contributed to understanding the emergent behavior of isolated quantum systems beyond the conventional equilibrium paradigm [7–23]. One approach to studying such non-equilibrium many-body systems is through quench dynamics. By using quench techniques, researchers can access novel exotic quantum states with energy levels significantly different from those of the ground state. These non-equilibrium states offer insights into the topological and superconducting properties of pre-quenched and post-quenched Hamiltonians [3]. Furthermore, the Loschmidt amplitudes

$$\mathcal{G}(t) = \prod_{0 < k < \pi} \langle \psi(t) | \psi(0) \rangle, \quad (1)$$

between the evolved state and initial states exhibit non-analytic behavior over time when the quench crosses a topological phase boundary. This phenomenon is referred to as dynamical quantum phase transition (DQPT) [25].

In this work, we investigate the non-equilibrium behavior of the general superconducting Kitaev chain with long-range couplings [26–32]. The model consists of spinless fermions capable of pairing up to form superconducting Cooper pairs with opposite momenta [33–49]. Typically, the topological phase boundaries of a general Kitaev chain are determined by the closing of the gap within the equilibrium paradigm. From the perspective of quantum quench dynamics, we decompose the study of non-equilibrium dynamics into an examination of an ensemble of free-pseudo spins under a magnetic field. The performance of the evolved state can be understood through the average spin precession. The topology of the driven Hamiltonian can be deduced from the average winding number of the evolved state. We demon-

strate that the singularity of the DQPT stems from two perpendicular pseudo-spin vectors belonging to the pre- and post-quenched Hamiltonians. We also analyze the distinct behaviors of the dynamic pairing order parameter in the topological and trivial regions based on the non-equilibrium pairing state generated from the vacuum state [3], which is defined as

$$\hat{\zeta}_k = -i \left(c_k^\dagger c_{-k} - c_k c_{-k} \right). \quad (2)$$

In the topological region, the order parameter associated with the pairing transition is independent of the chemical potential μ but decays as $|\mu|$ increases.

Our findings provide insights into the non-equilibrium behavior of topological superconductors and the interplay between quantum dynamics and topology. They have implications for understanding the robustness of topological properties in driven quantum systems and exploring novel phenomena in quantum information processing and condensed matter physics.

Model.—We examine the following generic Kitaev chain [1, 50].

$$H = \sum_{n=1}^M \sum_{j=1}^N (\kappa_n c_j^\dagger c_{j+n} + \Delta_n c_j^\dagger c_{j+n}^\dagger + \text{H.c.}) + \mu \sum_{j=1}^N (1 - 2c_j^\dagger c_j), \quad (3)$$

where c_j denotes the spinless fermion operator at the j th site with chemical potential μ , which is subject to periodic boundary conditions, i.e., $c_{N+n} = c_n$. Here κ_n represents long-range hopping and Δ_n represents the long-range pairing terms. This model has a rich phase diagram and serves as an extended one-dimensional mean-field representation of a triplet superconductor. By using the Fourier transformation $c_j = \frac{1}{\sqrt{N}} \sum_k e^{ikj} c_k$ and intro-

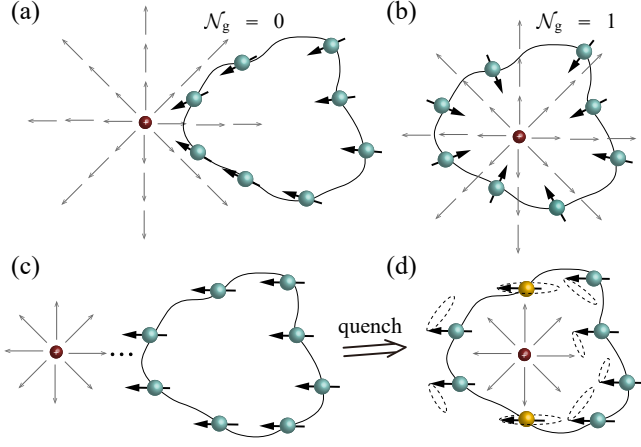


FIG. 1. Schematic representation of the ensemble of free pseudo spins under a magnetic field. The red solid circle represents the origin and can be considered as the monopole. (a)-(b) Different topologies of the Kitaev chain. The GS is formed by the direct product of the distinct pseudo-spin qubits. The corresponding pseudo-spin vector \mathbf{r}_g points in the opposite direction of the magnetic field. The topology of the system is determined by the winding number of \mathbf{r}_g . (c)-(d) The quench process employed in this work. The system is initially prepared in the topological trivial GS and subsequently quenched to the topological region. The yellow solid circle represents the special initial $\mathbf{r}_1(k_c)$, which is perpendicular to the local magnetic field of the post-quenched Hamiltonian. The dynamic behavior of the non-equilibrium state can be comprehended through the precession of each pseudo spin.

ducing the pseudo-spin operators

$$\begin{aligned} s_k^- &= (s_k^+)^\dagger = c_k c_{-k}, \\ s_k^z &= \frac{1}{2} (c_k^\dagger c_k + c_{-k}^\dagger c_{-k} - 1). \end{aligned} \quad (4)$$

The Hamiltonian can be expressed as,

$$H = \sum_{k>0} H_k = 4 \sum_{k>0} \mathbf{B}(k) \cdot \mathbf{s}_k. \quad (5)$$

Here the pseudo-spin operator $s_k^x = \frac{1}{2} (s_k^+ + s_k^-)$ and $s_k^y = \frac{1}{2i} (s_k^+ - s_k^-)$ satisfy commutation relations of the Lie algebra $[s_k^\alpha, s_{k'}^\beta] = 2\delta_{kk'} \epsilon_{\alpha\beta\gamma} s_{k'}^\gamma$, with $\epsilon_{\alpha\beta\gamma}$ Levi-Civita symbol, $\alpha, \beta, \gamma = x, y, z$. Additionally, $\mathbf{B}(k) = (0, \sum_{n=1}^M \Delta_n \sin(nk), \sum_{n=1}^M \kappa_n \cos(nk) - \mu)$ represents an external magnetic field that depends on the Bloch momentum (k) within the Brillouin zone (BZ). It is worth noting that the pseudo-spin representation of H differs slightly from the Pauli matrix representation used for a topological insulator. In this context, the pseudo-spin quantum number is $1/2$ (0) in the even-(odd-)parity subspace. In the following we focus on the even-parity subspace which involves quantum number $1/2$ for all $k > 0$, aligning with the parity symmetry of the generic Kitaev chain. We choose the s_k^z -basis, denoted as $\{|+, k\rangle =$

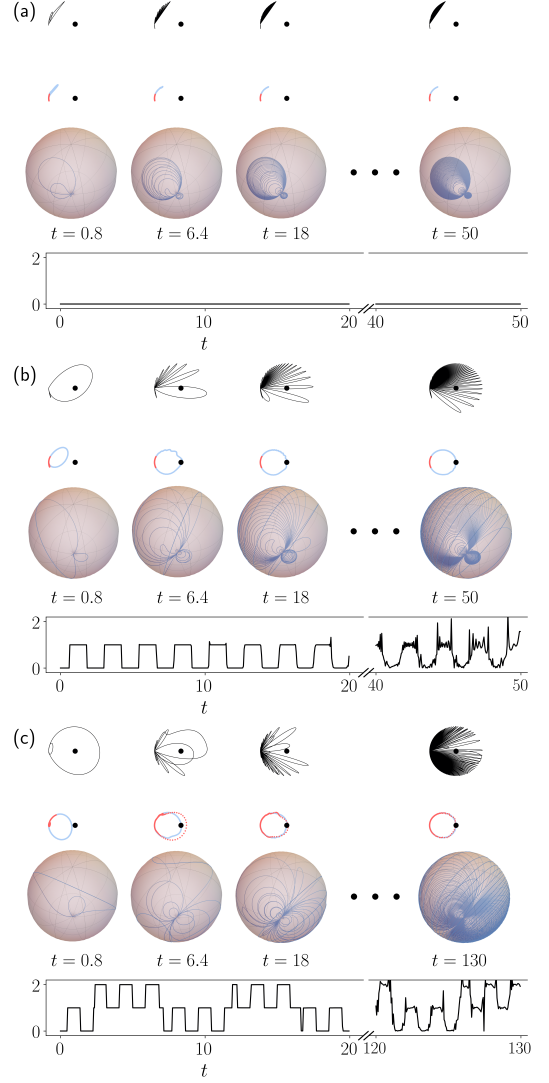


FIG. 2. Illustration of the evolution of pseudo-spin vectors after sudden quenching. The post-quench Hamiltonians have potentials μ of (a) 4, (b) 2, and (c) -0.5 , with winding numbers 0, 1, and 2 respectively. The loops of $r_x(k, t)$ and $r_y(k, t)$ are displayed in the first row of each subplot. The second row exhibits the plots of the $\bar{r}_\alpha(k, t)$. When $t \rightarrow \infty$, the Bloch vector stabilizes, offering valuable insights into the topology of the driven system, as illustrated on the right-hand side. To indicate the ranges, red dots represent $[0, \pi)$ and green dots represent $[\pi, 2\pi)$. Additionally, the third row presents 3D plots of the pseudo-spin vector's loop on the Bloch sphere. The fourth row provides a characterization of the instantaneous winding number corresponding to the instant loops in (a). The remaining parameters are $\Delta_1 = 1$, $\kappa_1 = 1$, $\Delta_2 = 1$, and $\kappa_2 = 2$.

$c_k^\dagger c_{-k}^\dagger |0\rangle, |-, k\rangle = |0\rangle\}$, where $|0\rangle$ represents the fermionic vacuum state.

We begin by elucidating how to extract topological information from the ground state via pseudo spins. As evidenced by the fact that $[H_k, H_{k'}] = 0$, we can describe

any state $|\psi\rangle = \prod_k |\psi\rangle_k$ within the subspace as an ensemble of interaction-free particles, each represented by the pseudo-spin vector $\mathbf{r}(k) = (\langle s_k^x \rangle, \langle s_k^y \rangle, \langle s_k^z \rangle)$, where $\langle s_k^\alpha \rangle = \langle \psi | s_k^\alpha | \psi \rangle_k$. Consequently, the Hamiltonian (5) can be interpreted as an ensemble of independent spins arranged on a loop under the influence of a 2D magnetic field generated by a Dirac monopole [52, 53], which has also been demonstrated in the previous studies [2, 55].

Based on this analysis, the ground state (GS) $|G\rangle$ and the phase diagram can be obtained. Each spin constituting the ground state aligns in the opposite direction of the k -dependent magnetic field, as shown in Figs. 1(a) and (b). Specifically, the vector for the ground state $\mathbf{r}_g(k)$ satisfies

$$\langle s_k^\alpha \rangle_g = \langle G | s_k^\alpha | G \rangle = -\frac{B_\alpha(k)}{2B(k)}. \quad (6)$$

Consequently, in the thermodynamic limit, the ground state energy density can be described as the integration of the absolute value of the magnetic field, given by $\varepsilon_g = \lim_{N \rightarrow \infty} \frac{E_g}{N} = -\frac{1}{2\pi} \int_0^\pi B(k) dk$. Simultaneously, $\mathbf{r}_g(k)$ can construct a closed curve in the yz -plane, with the associated winding number, indicating the total counterclockwise revolutions of the curve around a point,

$$\mathcal{N}_g = \frac{1}{2\pi} \int_c \frac{r_g^z dr_g^y - r_g^y dr_g^z}{r_g^2} \quad (7)$$

This winding number aligns with that derived from the Hamiltonian via $\mathbf{B}(k)$. Notably, the ground state energy density, which is dependent on the curve configuration, demonstrates nonanalytic behavior when the winding number of the corresponding loop changes. This observation highlights the relationship between the QPT and the geometric topological index that characterizes the phase diagram. In the SM [50], a comprehensive analysis is provided for various long-range Kitaev models and their associated geometric characteristics. Notably, the results presented in this paper exhibit a remarkable degree of generality, extending to arbitrary curves. This observation highlights the dynamic universality inherent in the long-range Kitaev model, rendering it applicable across a wide range of system configurations.

Dynamic Bloch vector.— We observe that the Bloch vector denoted as $\mathbf{r}_g(k)$, characterizes topological features of the ground state. This concept specifically describes the state itself, irrespective of its origin, such as the mother Hamiltonian. Hence, a natural question arises: can the Bloch vector detect features arising from quantum quenches in the Kitaev model, which differ from merely assessing a static quantity? To address this question, we initially focus on the pseudo-spin vector, which initially points to the north pole of the Bloch sphere ($\mathbf{r}(0) = \frac{1}{2}(0, 0, 1)$), and is subsequently influenced by a magnetic field $\mathbf{B} = B(\sin \theta \cos \varphi, \sin \theta \sin \varphi, \cos \theta)$. The time evolution of the pseudo-spin vector can be observed

as precession along the direction of the magnetic field, which is given by

$$\begin{aligned} \mathbf{r}(t) = & \frac{1}{2}(\sin 2Bt \sin \theta \sin \varphi + \sin^2 Bt \sin 2\theta \cos \varphi, \\ & -\sin 2Bt \sin \theta \cos \varphi + \sin^2 Bt \sin 2\theta \sin \varphi, \\ & 1 - \sin^2 Bt \sin^2 \theta). \end{aligned} \quad (8)$$

Therefore the average value of the pseudo-spin vector $\mathbf{r}(t)$ over an extended period of time, $\bar{\mathbf{r}}(t) = (\int_0^t \mathbf{r}(\tau) d\tau)/t$, can reflect the direction of the magnetic field, i.e., $\bar{\mathbf{r}}(\infty) \times \mathbf{B} = 0$. Indeed, $\bar{\mathbf{r}}(\infty)$ corresponds to the projection of $\mathbf{r}(0)$ onto the direction of the magnetic field.

With this approach in mind, we consider the following protocol [56, 57]: the initial state is the empty state in real space $|\psi(0)\rangle = \prod_{\pi > k > 0} |0\rangle_k |0\rangle_{-k} = \prod_l^N |0\rangle_N$. Each pseudo-spin vector within the corresponding spin ensemble points toward the $-z$ direction. This initial state lacks any information regarding the Hamiltonian. In a quantum quench experiment, such a system could be prepared in the ground state for infinite potential, i.e., $\mu \rightarrow \infty$ as shown in Fig. 1(c). Next, we introduce the post-quench Hamiltonian, $H(\mu_0)$ and for any given time t , the evolved state remains a tensor product state $|\psi(t)\rangle = \prod_{\pi > k > 0} |\psi_k(t)\rangle = \prod_{\pi > k > 0} \exp(-iH_k t) |\psi_k(0)\rangle$. A schematic illustration of the time evolution is plotted in Fig. 1(d). This indicates that every pseudo-spin vector rotates around the magnetic field at that point. Consequently, the ensemble $r_\alpha(k, t) = \langle \psi(t) | s_k^\alpha | \psi(t) \rangle$ allows us to extract the instantaneous winding number \mathcal{N}_t in the yz plane. This can be characterized by the last row of each subplot in Fig. 2. The time evolution of $\{\mathbf{r}(k, t)\}$ is presented in the third row of Fig. 2. Initially, at $t = 0$, it represents a point on the Bloch sphere, but for nonzero t , it transforms into a curve. As expected, the time-dependent curve exhibits high-frequency oscillations for large time values. Notably, although the corresponding winding number is not constant, it consistently oscillates around a certain value. This observation inspires us to average the oscillations by integrating them out [3]. Over an extended period, the rapidly oscillating term becomes negligible, resulting in a steady value given by

$$\begin{aligned} \bar{r}_\alpha^t(k, t) &= \frac{1}{t} \int_0^t r_\alpha(k, \tau) d\tau \quad (9) \\ \bar{r}_\alpha(k) &= \lim_{t \rightarrow \infty} \bar{r}_\alpha(k, t) = \langle s_k^\alpha \rangle_g \cos \theta_k. \end{aligned} \quad (10)$$

where $\theta_k = \cos^{-1}(B_z(k)/B(k))$. The loop of $\{\bar{\mathbf{r}}(k, t)\}$ is shown in the second row in Fig. 2. It is evident that the corresponding winding numbers of the pseudo-spin vectors $\{\bar{\mathbf{r}}(k)\}$ and $\{r_g(k)\}$ possess the same value. Therefore, the non-equilibrium steady value of $\{\bar{\mathbf{r}}(k)\}$ reveals the topology of the driven Hamiltonian. Indeed, averaging over a finite momentum shell $[k - \Delta k/2, k + \Delta k/2]$ for the pseudo-spin vector in the limit of large t yields

the same result, as mentioned in the SM [50]. This averaging over k helps eliminate the fast oscillation term and provides a more robust characterization of the system's properties.

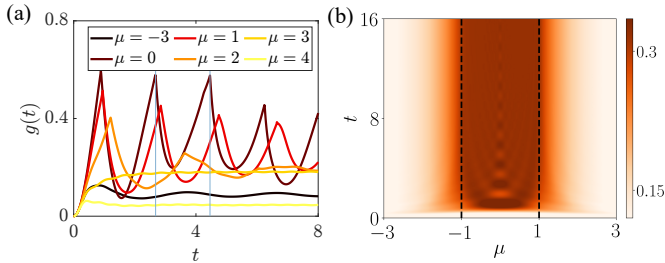


FIG. 3. (a) Dynamics of $g(t)$ defined in Eq. (11) following a quench in the generalized Kitaev model. Nonanalytic structures are observed when crossing the topological phase boundary ($\mu = 0, 1, 2$). The solid blue lines represent the time difference between two adjacent nonanalytic behaviors. The numerical result of 1.79 aligns with our analytical findings. The remaining parameters are $\Delta_1 = 1$, $\kappa_1 = 1$, $\Delta_2 = 1$, and $\kappa_2 = 2$. (b) Variation of the order parameter $\bar{\zeta}(t)$ as a function of t and μ . The plot demonstrates the tendency of the order parameter to stabilize within a plateau in the nontrivial topological region. The black dashed lines indicate the analytical behavior of the order parameter at the phase boundary.

Anatomy of the dynamical quantum phase transition.—DQPT is a concept that extends the notion of quantum phase transitions to coherent quantum real-time evolution [2, 3, 25, 58–60]. Here we examine the dynamical behavior of two observables to unravel their underlying mechanisms based on spin precession.

The first observable is the average natural logarithm of the $|\mathcal{G}(t)|^2$ in the large scale limit $N \rightarrow \infty$,

$$g(t) = - \lim_{N \rightarrow \infty} \log |\mathcal{G}(t)|^2 / N, \quad (11)$$

where $\mathcal{G}(t)$ is defined in Eq. (1). $g(t)$ exhibits non-analytic behavior when the quench process crosses the equilibrium topological phase boundary [2]. This phenomenon can be understood through spin precession. Let us consider the initial state $|\psi(0)\rangle$ which is prepared in the ground state of the Hamiltonian H with a winding number \mathcal{N} of 0. The corresponding pseudo-spin vector is denoted by $\{\mathbf{r}_I(k)\}$. The k -dependent magnetic field $\mathbf{B}_F(k)$ is extracted from the pseudo-spin vector of the ground state of the quenched Hamiltonian given by $\mathbf{B}_F(k) = -\mathbf{r}_F(k)$. For any sudden quench across the topological phase boundary, there must exist a k_c such that $\mathbf{r}_I(k_c) \perp \mathbf{r}_F(k_c)$ results in $\mathcal{G}_{k_c}(t_c) = 0$ with critical time $t_c = \pi(2n+1)/4B(k_c)$, which is represented by the yellow solid circle in Fig. 1(d). Fig. 3(a) illustrates a quenched process that demonstrates the nonanalytic behavior of $g(t)$. In this scenario, the system is initially prepared on the ground state for the initial potential and

then quenched to $H(\mu)$ with different values of μ . The numerical results of t_c correspond well with our analysis. The absence of DQPT is evidenced by the smooth and analytical evolution of the system, without any abrupt changes or singularities, as shown for $\mu = -3, 3, 4$ in Fig. 3(a).

The pairing is an additional observable of interest. Recent work [3] has examined two types of order parameters related to local pairing in real space and Bardeen-Cooper-Schrieffer (BCS)-like pairing in momentum space. A remaining question pertains to why the occurrence of topological region for the quench leads to the presence of order parameters and the underlying mechanism behind the nonanalytic behavior at the phase boundary. This phenomenon can be understood from the perspective of the pseudo-spin vector. For the sake of simplicity, we assume the system parameters of quenched Hamiltonian as $\kappa_1 = \delta_{n,1}$, and $\Delta_n = \delta_{n,1}\Delta$. Additionally, we recall the expressions for BCS-like pairing in momentum space, denoted as

$$\bar{\zeta}(t) = \frac{1}{t} \int_0^t \frac{\sum_{\pi > k > 0} |\langle \psi(t) | \hat{\zeta}_k | \psi(t) \rangle|}{N} d\tau, \quad (12)$$

with $\hat{\zeta}_k = -i(c_k^\dagger c_{-k} - c_k c_{-k})$ in the context of non-equilibrium dynamics [3]. Again the initial state, $|\psi(0)\rangle = \prod_l^N |0\rangle_N$, represents the GS of the pre-quenched topological trivial Hamiltonian in the coordinate space when $\mu \rightarrow \infty$. Straightforward algebra shows that $\bar{\zeta}(t) = \frac{1}{N} \sum_{\pi > k > 0} |F(k)| \left[1 - \frac{\sin(4|\mathbf{B}(k)|t)}{4|\mathbf{B}(k)|t} \right]$, where $F(k) = \bar{r}_y(k) \bar{r}_z(k) / |\bar{\mathbf{r}}(k)|^2$. We perform the numerical simulation in Fig. 3(b). In the thermodynamic limit, it can be expressed as follows: $\zeta(\infty) = \frac{1}{4\pi} \int_0^\pi |\sin 2\vartheta_k| dk$, where $\vartheta_k = \sin^{-1}[\bar{r}_y(k) / |\bar{\mathbf{r}}(k)|]$. By considering the contribution of the pseudo-spin vector with the same $\sin \vartheta_k$, the integral can be transformed to $\zeta(\infty) = \frac{1}{2\pi} \int_0^\Theta |\sin 2\vartheta_k| d\varphi_k$, with $\tan \vartheta_k = \Delta \tan \varphi_k$. When the post-quenched Hamiltonian resides in the nontrivial region, the upper limit $\Theta = \pi/2$, allows $\zeta(\infty)$ to attain a value independent of μ . However, in the case of the post-quenched Hamiltonian being in the topologically trivial region, Θ needs to be expressed as a function of μ . Furthermore, the analytic behavior of $\zeta(\infty)$ serves as a means to characterize the quantum phase transition. For more detailed information, please refer to the SM [50].

Summary and discussion.—In this letter, we explore the non-equilibrium behavior of the Kitaev model with long-range couplings using a quantum quench dynamics approach. We investigate an ensemble of free-pseudo spins subjected to a magnetic field. The performance of the evolved state is analyzed by studying the average spin precession, and the topology of the driven Hamiltonian is determined through examination of the average winding number of the evolved state. We demonstrate the generation of a stable non-equilibrium pairing state starting

from an initial vacuum state. Furthermore, we establish that the singularity of the DQPT arises from two perpendicular pseudo-spin vectors associated with the pre- and post-quenched Hamiltonians. We also analyze the distinctive behaviors of the dynamic pairing order parameter in both topological and nontopological regions. These findings offer valuable insights into the non-equilibrium behavior of topological superconductors, providing implications for understanding the resilience of topological properties in driven quantum systems. In future research, we aim to extend our investigation to other models exhibiting similar characteristics, aiming to broaden our understanding of non-equilibrium behavior and uncover potential universality and scaling laws.

We acknowledge the support of the National Natural Science Foundation of China (Grants No. 12275193, No. 11975166, and No. 12374461).

* zhangxz@tjnu.edu.cn

† songtc@nankai.edu.cn

- [1] P. Calabrese, F. H. Essler, and M. Fagotti, Quantum quench in the transverse-field ising chain, *Physical review letters* **106**, 227203 (2011).
- [2] M. Heyl, A. Polkovnikov, and S. Kehrein, Dynamical quantum phase transitions in the transverse-field ising model, *Physical review letters* **110**, 135704 (2013).
- [3] M. Heyl, Dynamical quantum phase transitions: a review, *Reports on Progress in Physics* **81**, 054001 (2018).
- [4] J. Marino, M. Eckstein, M. S. Foster, and A. M. Rey, Dynamical phase transitions in the collisionless pre-thermal states of isolated quantum systems: theory and experiments, *Reports on Progress in Physics* **85**, 116001 (2022).
- [5] B.-W. Li, Y.-K. Wu, Q.-X. Mei, R. Yao, W.-Q. Lian, M.-L. Cai, Y. Wang, B.-X. Qi, L. Yao, L. He, *et al.*, Probing critical behavior of long-range transverse-field ising model through quantum kibble-zurek mechanism, *PRX Quantum* **4**, 010302 (2023).
- [6] V. Alba and P. Calabrese, Entanglement dynamics after quantum quenches in generic integrable systems, *SciPost Physics* **4**, 017 (2018).
- [7] P. Jurcevic, H. Shen, P. Hauke, C. Maier, T. Brydges, C. Hempel, B. Lanyon, M. Heyl, R. Blatt, and C. Roos, Direct observation of dynamical quantum phase transitions in an interacting many-body system, *Physical review letters* **119**, 080501 (2017).
- [8] J. Zhang, G. Pagano, P. W. Hess, A. Kyprianidis, P. Becker, H. Kaplan, A. V. Gorshkov, Z.-X. Gong, and C. Monroe, Observation of a many-body dynamical phase transition with a 53-qubit quantum simulator, *Nature* **551**, 601 (2017).
- [9] C. Monroe, W. C. Campbell, L.-M. Duan, Z.-X. Gong, A. V. Gorshkov, P. W. Hess, R. Islam, K. Kim, N. M. Linke, G. Pagano, *et al.*, Programmable quantum simulations of spin systems with trapped ions, *Reviews of Modern Physics* **93**, 025001 (2021).
- [10] R. Blatt and C. F. Roos, Quantum simulations with trapped ions, *Nature Physics* **8**, 277 (2012).
- [11] M. Schreiber, S. S. Hodgman, P. Bordia, H. P. Lüschen, M. H. Fischer, R. Vosk, E. Altman, U. Schneider, and I. Bloch, Observation of many-body localization of interacting fermions in a quasirandom optical lattice, *Science* **349**, 842 (2015).
- [12] H. Bernien, S. Schwartz, A. Keesling, H. Levine, A. Omran, H. Pichler, S. Choi, A. S. Zibrov, M. Endres, M. Greiner, *et al.*, Probing many-body dynamics on a 51-atom quantum simulator, *Nature* **551**, 579 (2017).
- [13] S. Choi, J. Choi, R. Landig, G. Kucsko, H. Zhou, J. Isoya, F. Jelezko, S. Onoda, H. Sumiya, V. Khemani, *et al.*, Observation of discrete time-crystalline order in a disordered dipolar many-body system, *Nature* **543**, 221 (2017).
- [14] A. Wallraff, D. Schuster, A. Blais, L. Frunzio, R.-S. Huang, J. Majer, S. Kumar, S. Girvin, and R. Schoelkopf, Circuit quantum electrodynamics: Coherent coupling of a single photon to a cooper pair box, *arXiv preprint cond-mat/0407325* (2004).
- [15] K. Xu, Z.-H. Sun, W. Liu, Y.-R. Zhang, H. Li, H. Dong, W. Ren, P. Zhang, F. Nori, D. Zheng, *et al.*, Probing dynamical phase transitions with a superconducting quantum simulator, *Science advances* **6**, eaba4935 (2020).
- [16] D. Chang, J. Douglas, A. González-Tudela, C.-L. Hung, and H. Kimble, Colloquium: Quantum matter built from nanoscopic lattices of atoms and photons, *Reviews of Modern Physics* **90**, 031002 (2018).
- [17] J. Ye, H. Kimble, and H. Katori, Quantum state engineering and precision metrology using state-insensitive light traps, *science* **320**, 1734 (2008).
- [18] J.-M. Raimond, M. Brune, and S. Haroche, Manipulating quantum entanglement with atoms and photons in a cavity, *Reviews of Modern Physics* **73**, 565 (2001).
- [19] M. Gring, M. Kuhnert, T. Langen, T. Kitagawa, B. Rauer, M. Schreitl, I. Mazets, D. A. Smith, E. Demler, and J. Schmiedmayer, Relaxation and prethermalization in an isolated quantum system, *Science* **337**, 1318 (2012).
- [20] B. Neyenhuis, J. Zhang, P. W. Hess, J. Smith, A. C. Lee, P. Richerme, Z.-X. Gong, A. V. Gorshkov, and C. Monroe, Observation of prethermalization in long-range interacting spin chains, *Science advances* **3**, e1700672 (2017).
- [21] J. Smith, A. Lee, P. Richerme, B. Neyenhuis, P. W. Hess, P. Hauke, M. Heyl, D. A. Huse, and C. Monroe, Many-body localization in a quantum simulator with programmable random disorder, *Nature Physics* **12**, 907 (2016).
- [22] J.-Y. Choi, S. Hild, J. Zeiher, P. Schauß, A. Rubio-Abadal, T. Yefsah, V. Khemani, D. A. Huse, I. Bloch, and C. Gross, Exploring the many-body localization transition in two dimensions, *Science* **352**, 1547 (2016).
- [23] J. Zhang, P. W. Hess, A. Kyprianidis, P. Becker, A. Lee, J. Smith, G. Pagano, I.-D. Potirniche, A. C. Potter, A. Vishwanath, *et al.*, Observation of a discrete time crystal, *Nature* **543**, 217 (2017).
- [3] Y. Shi, K. Zhang, and Z. Song, Dynamic generation of nonequilibrium superconducting states in a kitaev chain, *Physical Review B* **106**, 184505 (2022).
- [25] M. Heyl, Scaling and universality at dynamical quantum phase transitions, *Physical Review Letters* **115**, 140602 (2015).
- [26] A. Altland and M. R. Zirnbauer, Nonstandard symmetry classes in mesoscopic normal-superconducting hybrid structures, *Physical Review B* **55**, 1142 (1997).
- [27] A. Y. Kitaev, Unpaired majorana fermions in quantum wires, *Physics-uspekhi* **44**, 131 (2001).
- [28] A. Soori, Majorana fermions in kitaev chains side-coupled

- to normal metals, [arXiv preprint arXiv:2403.02266 \(2024\)](#).
- [29] K. Decker and C. Karrasch, Density matrix renormalization group study of the interacting kitaev chain with quasi-periodic disorder, [The European Physical Journal B **97**, 115 \(2024\)](#).
- [30] M. Malard and D. S. Brandão, Detecting and leaking a majorana bound state through proximity to a kitaev ring, [arXiv preprint arXiv:2403.01588 \(2024\)](#).
- [31] E. Silva, R. B. Ribeiro, H. Caldas, and M. A. Continentino, Hybridization induced triplet superconductivity with $s_z = 0$, [Physical Review B **109**, 134503 \(2024\)](#).
- [32] E. Starchl and L. M. Sieberer, Relaxation to a parity-time symmetric generalized gibbs ensemble after a quantum quench in a driven-dissipative kitaev chain, [Physical Review Letters **129**, 220602 \(2022\)](#).
- [33] D. Vodola, L. Lepori, E. Ercolessi, A. V. Gorshkov, and G. Pupillo, Kitaev chains with long-range pairing, [Physical review letters **113**, 156402 \(2014\)](#).
- [34] D. Vodola, L. Lepori, E. Ercolessi, and G. Pupillo, Long-range ising and kitaev models: phases, correlations and edge modes, [New Journal of Physics **18**, 015001 \(2015\)](#).
- [35] O. Viyuela, D. Vodola, G. Pupillo, and M. A. Martin-Delgado, Topological massive dirac edge modes and long-range superconducting hamiltonians, [Physical Review B **94**, 125121 \(2016\)](#).
- [36] L. Lepori and L. Dell'Anna, Long-range topological insulators and weakened bulk-boundary correspondence, [New Journal of Physics **19**, 103030 \(2017\)](#).
- [37] U. Bhattacharya, S. Maity, A. Dutta, and D. Sen, Critical phase boundaries of static and periodically kicked long-range kitaev chain, [Journal of Physics: Condensed Matter **31**, 174003 \(2019\)](#).
- [38] T. Koffel, M. Lewenstein, and L. Tagliacozzo, Entanglement entropy for the long-range ising chain in a transverse field, [Physical review letters **109**, 267203 \(2012\)](#).
- [39] P. Hauke and L. Tagliacozzo, Spread of correlations in long-range interacting quantum systems, [Physical review letters **111**, 207202 \(2013\)](#).
- [40] T. Graß and M. Lewenstein, Trapped-ion quantum simulation of tunable-range heisenberg chains, [EPJ Quantum Technology **1**, 1 \(2014\)](#).
- [41] A. Dutta and A. Dutta, Probing the role of long-range interactions in the dynamics of a long-range kitaev chain, [Physical Review B **96**, 125113 \(2017\)](#).
- [42] S. Vajna and B. Dóra, Topological classification of dynamical phase transitions, [Physical Review B **91**, 155127 \(2015\)](#).
- [43] N. Sedlmayr, P. Jaeger, M. Maiti, and J. Sirker, Bulk-boundary correspondence for dynamical phase transitions in one-dimensional topological insulators and superconductors, [Physical Review B **97**, 064304 \(2018\)](#).
- [44] T. Maslowski and N. Sedlmayr, Dynamical bulk-boundary correspondence and dynamical quantum phase transitions in higher-order topological insulators, [Physical Review B **108**, 094306 \(2023\)](#).
- [45] H. Cheraghi and N. Sedlmayr, Dynamical quantum phase transitions following double quenches: persistence of the initial state vs dynamical phases, [New Journal of Physics **25**, 103035 \(2023\)](#).
- [46] K. Sim, R. Chitra, and P. Mognini, Quench dynamics and scaling laws in topological nodal loop semimetals, [Physical Review B **106**, 224302 \(2022\)](#).
- [47] P. Mognini, E. van Nieuwenburg, and R. Chitra, Sensing floquet-majorana fermions via heat transfer, [Physical Review B **96**, 125144 \(2017\)](#).
- [48] P. Mognini, W. Chen, and R. Chitra, Universal quantum criticality in static and floquet-majorana chains, [Physical Review B **98**, 125129 \(2018\)](#).
- [49] P. Mognini, Edge mode manipulation through commensurate multifrequency driving, [Physical Review B **102**, 235143 \(2020\)](#).
- [50] See Supplemental Material for the details on configuration of pseudo spin and topology (Sec. A), derivation of dynamics of the Bloch vector and dynamical topological characterization (Sec. B) as well as the order parameter (Sec. C).
- [1] T. Suzuki, T. Someya, T. Hashimoto, S. Michimae, M. Watanabe, M. Fujisawa, T. Kanai, N. Ishii, J. Itatani, S. Kasahara, *et al.*, Photoinduced possible superconducting state with long-lived disproportionate band filling in fese, [Communications Physics **2**, 115 \(2019\)](#).
- [52] P. A. M. Dirac, Quantised singularities in the electromagnetic field, [Proceedings of the Royal Society of London. Series A, Containing Papers of a Mathematical and Physical Character **133**, 60 \(1931\)](#).
- [53] R. A. Barankov and L. S. Levitov, Synchronization in the bcs pairing dynamics as a critical phenomenon, [Physical review letters **96**, 230403 \(2006\)](#).
- [2] G. Zhang, C. Li, and Z. Song, Majorana charges, winding numbers and chern numbers in quantum ising models, [Scientific Reports **7**, 8176 \(2017\)](#).
- [55] G. Zhang and Z. Song, Topological characterization of extended quantum ising models, [Physical review letters **115**, 177204 \(2015\)](#).
- [56] W. DeGottardi, D. Sen, and S. Vishveshwara, Topological phases, majorana modes and quench dynamics in a spin ladder system, [New Journal of Physics **13**, 065028 \(2011\)](#).
- [57] U. Mishra, R. Jafari, and A. Akbari, Disordered kitaev chain with long-range pairing: Loschmidt echo revivals and dynamical phase transitions, [Journal of Physics A: Mathematical and Theoretical **53**, 375301 \(2020\)](#).
- [58] D. Mondal and T. Nag, Finite-temperature dynamical quantum phase transition in a non-hermitian system, [Physical Review B **107**, 184311 \(2023\)](#).
- [59] A. K. Ghosh, A. Saha, and T. Nag, Corner modes in non-hermitian long-range model, [arXiv preprint arXiv:2403.19765 \(2024\)](#).
- [60] D. Mondal and T. Nag, Persistent anomaly in dynamical quantum phase transition in long-range non-hermitian p-wave kitaev chain, [The European Physical Journal B **97**, 59 \(2024\)](#).

SUPPLEMENTAL MATERIAL

Y. B. Shi,¹ X. Z. Zhang,^{2,*} and Z. Song^{1,†}

¹*School of Physics, Nankai University, Tianjin 300071, China*

²*College of Physics and Materials Science, Tianjin Normal University, Tianjin 300387, China*

*zhangxz@tjnu.edu.cn

†songtc@nankai.edu.cn

In this Supplemental Material, we present **A.** Configuration of pseudo spin and topology; **B.** Derivation of dynamics of the Bloch vector and dynamical topological characterization; and **C.** Derivation of the order parameter $\bar{\zeta}$.

A. Configuration of pseudo spin and topology

In the main text, we present the extensive topological properties of the long-range Kitaev model through its geometric characterization. Within this subsection, we explicitly demonstrate this phenomenon by examining specific Hamiltonians in coordinate space. The Hamiltonian of the generalized Kitaev chain is the same as Eq. (3) in the main text

$$H = \sum_{n=1}^M \sum_{j=1}^N (\kappa_n c_j^\dagger c_{j+n} + \Delta_n c_j^\dagger c_{j+n}^\dagger + \text{H.c.}) + \mu \sum_{j=1}^N (1 - 2c_j^\dagger c_j), \quad (\text{S1})$$

where c_j represents the spinless fermion operator at the j th site with chemical potential μ , and it obeys periodic boundary conditions, i.e., $c_{N+n} = c_n$. This model serves as an extended one-dimensional mean-field representation of a triplet superconductor, incorporating long-range hopping and pairing terms with strengths κ_n and Δ_n , respectively. In the limit of large N with $M \ll N$, the Hamiltonian can be mapped to a one-dimensional quantum spin model [1] using the conventional Jordan-Wigner transformation,

$$c_j = \prod_{i=1}^{j-1} (-\sigma_i^z) \sigma_j^-, c_j^\dagger = \prod_{i=1}^{j-1} (-\sigma_i^z) \sigma_j^+. \quad (\text{S2})$$

By employing the Fourier transformation,

$$c_j = \frac{1}{\sqrt{N}} \sum_k e^{ikj} c_k, \quad (\text{S3})$$

the total Hamiltonian H can be block diagonalized as

$$H = \sum_{k>0} H_k, \quad (\text{S4})$$

satisfying $[H_k, H_{k'}] = 0$ and H_k is given by,

$$H_k = -2i \sum_{n=1}^M \Delta_n \sin(nk) c_{-k}^\dagger c_k^\dagger + \text{h.c.} + 2 \left(\sum_{n=1}^M \kappa_n \cos(nk) - \mu \right) (c_k^\dagger c_k + c_{-k}^\dagger c_{-k}) - 2\mu. \quad (\text{S5})$$

When we introduce the pseudo-spin operators,

$$\begin{aligned} s_k^- &= (s_k^+)^\dagger = c_k c_{-k}, \\ s_k^z &= \frac{1}{2} (c_k^\dagger c_k + c_{-k}^\dagger c_{-k} - 1), \end{aligned} \quad (\text{S6})$$

the Hamiltonian H_k can be expressed as

$$H_k = 4 \left(\sum_{n=1}^M \kappa_n \cos(nk) - \mu \right) s_k^z - 2i \sum_{n=1}^M \Delta_n \sin(nk) s_k^+ + 2i \sum_{n=1}^M \Delta_n \sin(nk) s_k^- \quad (\text{S7})$$

$$= 4\mathbf{B}(k) \cdot \mathbf{s}_k, \quad (\text{S8})$$

with the field $B(k) = (0, \sum_{n=1}^M \Delta_n \sin(nk), \sum_{n=1}^M \kappa_n \cos(nk) - \mu)$. The pseudo-spin operators $s_k^x = \frac{1}{2}(s_k^+ + s_k^-)$ and $s_k^y = \frac{1}{2i}(s_k^+ - s_k^-)$ follow the commutation relations of the Lie algebra $[s_k^\alpha, s_{k'}^\beta] = 2\delta_{kk'}\epsilon_{\alpha\beta\gamma}s_k^\gamma$, where $\epsilon_{\alpha\beta\gamma}$ denotes the Levi-Civita symbol and $\alpha, \beta,$ and γ take on values of $x, y,$ and z .

This conclusion applies to the generalized model at hand, which corresponds to a loop traced by the parametric equation $\mathbf{B}(k)$. In general, the winding number of a closed curve in the auxiliary yz -plane around the origin is defined as $\mathcal{N} = \frac{1}{2\pi} \int_c \frac{1}{r^2} (zdy - ydz)$, an integer representing the total number of times the curve travels anticlockwise around the origin. The connection between the quantum phase transition and the switch of the topological quantity has been established by considering $\mathbf{r}(k) = \mathbf{B}(k)$ [2].

Alternatively, one can introduce a vector $\mathbf{r}_g(k) = (\langle s_k^x \rangle_g, \langle s_k^y \rangle_g, \langle s_k^z \rangle_g)$ with

$$\langle s_k^\alpha \rangle_g = \langle G | s_k^\alpha | G \rangle = -\frac{B_\alpha(k)}{2B(k)}. \quad (\text{S9})$$

The corresponding winding number \mathcal{N}_g can be obtained by considering $\mathbf{r}(k) = (\langle s_k^x \rangle_g, \langle s_k^y \rangle_g, \langle s_k^z \rangle_g)$. Notably, both vectors $\mathbf{r}_g(k)$ and $\mathbf{B}(k)$ share the same winding number. In parallel, $r_g(k) = |\mathbf{r}_g(k)|$ plays a similar role to $B(k)$ in characterizing the occurrence of a quantum phase transition.

Considering the nonzero parameters as $\kappa_1 = 1$ and $\Delta_1 = 1$, the vector $\mathbf{r}_g(k) = \left(0, \frac{\sin k}{2\sqrt{1-2\mu \cos k + \mu^2}}, \frac{\cos k - \mu}{2\sqrt{1-2\mu \cos k + \mu^2}}\right)$ represents a circle. The winding numbers associated with it are 0 and 1, depending on the value of μ . Similarly, when $\kappa_1 = 1, \kappa_2 = 2, \Delta_1 = 1,$ and $\Delta_2 = 1$, the vector $\mathbf{r}_g(k) = \left(0, \frac{\sin k + \sin 2k}{2|\mathbf{B}|}, \frac{\cos k + 2\cos 2k - \mu}{2|\mathbf{B}|}\right)$ represents a trefoil. The trefoil has winding numbers of 0, 1, and 2. Here, $|\mathbf{B}| = \sqrt{\mu^2 - 2(2\cos 2k + \cos k)\mu + 4\cos^3 k + 3\cos^2 2k + 2}$. Figs. S1(a) and (b) illustrate two such typical cases, which will be also employed to demonstrate the subsequent quench dynamics. It is worth pointing out that the correspondence between the GS and free spin subjected to the magnetic field is held for any given geometric curve. For diversity, we give two complex examples in Figs. S1(c) and (d).

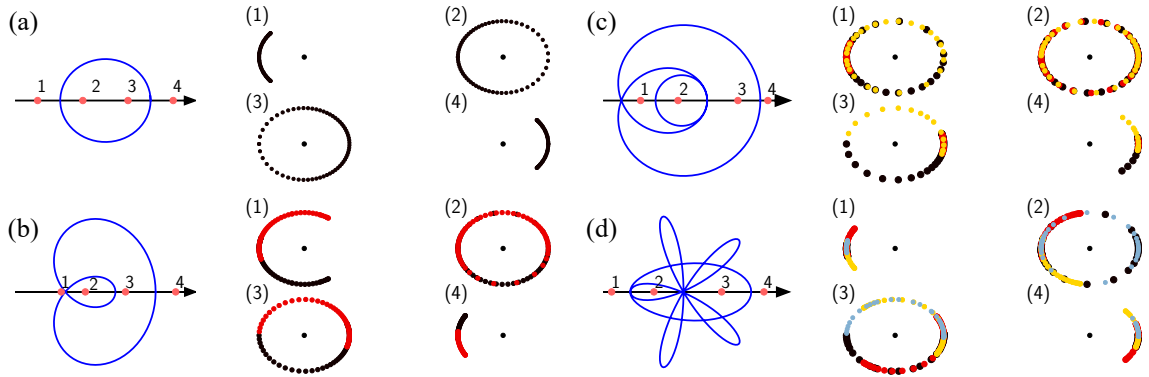


FIG. S1. Geometric representation of the GS of the long-range Kitaev model in the parametric space. The left panel of each figure illustrates the curve of the GS, which is determined by Eq. (S9). The red circle represents the origin of the parametric space, which determines the topology of the Hamiltonian. The right panel shows the curve when the origin is determined. The corresponding parameters are as follows: (a) $\kappa_1 = 1$ and $\Delta_1 = 1$. The black points on the right panel indicate the range of momentum k from $(0, 2\pi]$. The locations of the origins defined by the red circles are $\mu = -1.5, -0.5, 0.5,$ and 1.5 , respectively. (b) $\kappa_1 = 1, \kappa_2 = 2, \Delta_1 = 1,$ and $\Delta_2 = 1$. The black and red points on the right panel represent the range of momentum k from $(0, \pi]$ and $(\pi, 2\pi]$, respectively. The origins of four typical cases are determined by $\mu = -1.7, -0.5, 1.5,$ and 4 , respectively. (c) $\kappa_1 = 1, \kappa_2 = 4, \kappa_3 = 6, \Delta_1 = 1, \Delta_2 = 2,$ and $\Delta_3 = 3$. The black, red, and yellow points indicate the range of momentum k from $(0, \frac{2}{3}\pi], (\frac{2}{3}\pi, \frac{4}{3}\pi],$ and $(\frac{4}{3}\pi, 2\pi]$, respectively. The corresponding μ values are $-5, 0, 8,$ and 12 , respectively. (d) $\kappa_1 = 1, \kappa_2 = -2, \kappa_3 = 7, \kappa_4 = 9, \Delta_1 = 1, \Delta_2 = 2, \Delta_3 = -3,$ and $\Delta_4 = 4$. The black, red, yellow, and blue points represent the range of momentum k from $(0, \frac{1}{2}\pi], (\frac{1}{2}\pi, \pi], (\pi, \frac{3}{2}\pi],$ and $(\frac{3}{2}\pi, 2\pi]$, respectively. The value of μ is $-18, -8, 8,$ and 18 , respectively. The different colors highlight the larger winding number of the curve.

B. Derivation of dynamics of the Bloch vector and dynamical topological characterization

In the previous section, we have demonstrated the utility of the Bloch vector $\mathbf{r}_g(k)$ in characterizing the quantum phase diagram and topological properties of the ground state. Importantly, this concept solely focuses on the state itself, disregarding its origin, which is the mother Hamiltonian. Generally, it provides insights into the characteristics of the associated Hamiltonian, especially when the state corresponds to the ground state. Consequently, an important question arises: Can the Bloch vector extracted from a time-evolved state effectively capture the features of the driven Hamiltonian? We provide an affirmative answer. In this section, we present two possible methods for detecting the pseudo-spin vectors. First, we introduce a time-dependent Bloch-like vector denoted as

$$\langle s_k^\alpha \rangle_t = \langle \psi(t) | s_k^\alpha | \psi(t) \rangle, \quad (\text{S10})$$

which is defined as the expectation value of the pseudo-spin operator s_k^α for the evolved state $|\psi(t)\rangle = e^{-iHt} |\psi(0)\rangle = \prod_{\pi>k>0} e^{-iH_k t} |0\rangle_k |0\rangle_{-k}$. This vector represents a well-defined set of values and the instantaneous winding number \mathcal{N}_t can be obtained by considering the components $\{\mathbf{r}(k) = (\langle s_k^x \rangle_t, \langle s_k^y \rangle_t, \langle s_k^z \rangle_t)\}$. In Fig. 2 of the main text, the time-dependent curve exhibits high-frequency oscillations for large time values. It is worth noting that although the corresponding winding number is not constant, it consistently oscillates around a specific value. This observation motivates us to perform an averaging procedure to eliminate the oscillations. In the following, we will explore two different approaches for averaging: (i) averaging over a long time interval t and (ii) averaging over a finite momentum shell $[k - \Delta k/2, k + \Delta k/2]$.

First, taking the average over a period of time t , we obtain a t -dependent vector denoted as

$$\bar{r}_\alpha^t(k, t) = \frac{1}{t} \int_0^t \langle s_k^\alpha \rangle_\tau d\tau. \quad (\text{S11})$$

A straightforward derivation yields the following expression for the state vector $|\psi(t)\rangle$

$$|\psi(t)\rangle = \left[\cos(2|\mathbf{B}|t) + i \frac{B_z}{|\mathbf{B}|} \sin(2|\mathbf{B}|t) \right] |0\rangle_k |0\rangle_{-k} - \frac{B_y}{|\mathbf{B}|} \sin(2|\mathbf{B}|t) |1\rangle_k |1\rangle_{-k}. \quad (\text{S12})$$

Based on the evolved state, we express the set of pseudo-spin vectors at each time as follows

$$\begin{aligned} \langle s_k^x \rangle_t &= -\frac{B_y}{|\mathbf{B}|} \sin(4|\mathbf{B}|t), \\ \langle s_k^y \rangle_t &= -\frac{B_y B_z}{|\mathbf{B}|^2} \sin^2(2|\mathbf{B}|t), \\ \langle s_k^z \rangle_t &= \frac{B_y^2}{|\mathbf{B}|^2} \sin^2(2|\mathbf{B}|t) - \frac{1}{2}. \end{aligned} \quad (\text{S13})$$

By substituting these equations into Eq. (S11), we readily obtain the expressions for $\bar{r}_\alpha^t(k, t)$, i.e.,

$$\begin{aligned} \bar{r}_x^t(k, t) &= \frac{B_y \cos(4|\mathbf{B}|t) - 1}{|\mathbf{B}| 4|\mathbf{B}|t}, \\ \bar{r}_y^t(k, t) &= \frac{B_y B_z \sin(4|\mathbf{B}|t)}{8|\mathbf{B}|^3 t} - \frac{B_y B_z}{2|\mathbf{B}|^2}, \\ \bar{r}_z^t(k, t) &= -\frac{B_y^2 \sin(4|\mathbf{B}|t)}{8|\mathbf{B}|^3 t} - \frac{B_z^2}{2|\mathbf{B}|^2}. \end{aligned} \quad (\text{S14})$$

In the limit as $t \rightarrow \infty$, we have

$$\bar{r}_\alpha^t(k) = \lim_{t \rightarrow \infty} \bar{r}_\alpha^t(k, t) = \langle s_k^\alpha \rangle_g \cos \theta_k. \quad (\text{S15})$$

In this context, $\theta_k = \cos^{-1}\left(\frac{B_z(k)}{B(k)}\right)$ represents the angle between the initial Bloch vector and the magnetic field dependent on k . Moreover, the winding numbers of the two vectors $\bar{r}_\alpha(k)$ and $\langle s_k^\alpha \rangle_g$ possess the same value.

Next, we average each pseudo-spin vector over a finite momentum shell $[k - \Delta k/2, k + \Delta k/2]$, given by

$$\bar{r}_\alpha^k(k_0, t) = \frac{1}{2\Delta k} \int_{k_0 - \Delta k}^{k_0 + \Delta k} \langle s_k^\alpha \rangle_t dk, \quad (\text{S16})$$

where $k \gg \Delta k \gg dk$. In the limit of large time t ,

$$\begin{aligned}\bar{r}_x^k(k_0, t) &\approx \frac{B_y}{8\Delta kt |\mathbf{B}|} [\cos(4|\mathbf{B}|(k_0 + \Delta k)t) - \cos(4|\mathbf{B}|(k_0 - \Delta k)t)] \frac{dk}{d|\mathbf{B}|} \Big|_{k=k_0}, \\ \bar{r}_x^k(k_0, t) &\approx \frac{B_y B_z}{16|\mathbf{B}|^2 \Delta kt} [\sin(4|\mathbf{B}|(k_0 + \Delta k)t) - \sin(4|\mathbf{B}|(k_0 - \Delta k)t)] \frac{dk}{d|\mathbf{B}|} \Big|_{k=k_0} - \frac{B_y B_z}{2|\mathbf{B}|^2}, \\ \bar{r}_x^k(k_0, t) &\approx -\frac{B_y^2}{16|\mathbf{B}|^2 \Delta kt} [\sin(4|\mathbf{B}|(k_0 + \Delta k)t) - \sin(4|\mathbf{B}|(k_0 - \Delta k)t)] \frac{dk}{d|\mathbf{B}|} \Big|_{k=k_0} - \frac{B_z^2}{2|\mathbf{B}|^2}.\end{aligned}\quad (\text{S17})$$

Neglecting the high-frequency oscillating term yields the same result as $\bar{r}_\alpha^t(k, t)$,

$$\bar{r}_\alpha^k(k) = \lim_{T \rightarrow \infty} \bar{r}_\alpha^k(k, T) = \langle s_k^\alpha \rangle_g \cos \theta_k. \quad (\text{S18})$$

We consider the value of Δk is proportional to $1/N$ and the value of dk equals $2\pi/N$ in the numerical simulation. In Fig. S2, we present the ensembles $\{\bar{r}_\alpha^t(k, t)\}$ and $\{\bar{r}_\alpha^k(k, t)\}$ at different times. The collection of curves depicted in Fig. S2 demonstrates that both of these distinct averaging approaches serve a common purpose and effectively reveal the topology of the driven Hamiltonian, aligning with the analytical results presented in Eqs. (S15) and (S18). At the same time, employing longer time intervals for averaging, denoted as t , leads to faster stabilization. The difference in the time scales at which the two methods converge to stability is influenced by the parameter Δk , as evident in Eqs. (S14) and (S17). Moreover, this approach has the potential to facilitate experimental measurements by providing a simplified and accessible method for evaluating the order parameter.

Next, we consider two special conditions, one with non-uniform on-site potential and the other with non-uniform coupling strengths. The numerical simulation for the first condition is shown in Fig. S3. In Fig. S3(a) and S3(b), we use the same parameters as in Fig. S2, but with on-site disorder within the range $[-\delta, \delta]$. We choose different values of μ to consider different systems whose ground states have different winding numbers. In Fig. S3(c), we also plot the time-averaged $\{\bar{r}_\alpha^t(k, t)\}$ for the extended version of the system in Fig. S1(c) with disorder. For the second condition, we consider the inverse-square decaying coupling strengths, i.e.,

$$\kappa_n = \frac{1}{n^2}, \Delta_1 = 1.$$

The numerical simulation is performed in Fig. S4. They all demonstrate the robustness and universality of our approach.

C. Derivation of the order parameter $\bar{\zeta}$

The consistent outcome of the two distinct averaging approaches after an extended period in the previous section prompts us to consider whether the instantaneous order parameter,

$$\zeta(t) = \frac{\sum_{\pi > k > 0} |\langle \psi(t) | \hat{\zeta}_k | \psi(t) \rangle|}{N}, \quad (\text{S19})$$

will eventually show the same expression as the time-averaged order parameter $\bar{\zeta}(t)$? To answer this question we decompose $\zeta(t)$ into two parts,

$$\zeta(t) = \zeta(\infty) - \delta\zeta(t), \quad (\text{S20})$$

where

$$\zeta(\infty) = \frac{1}{2\pi} \int_0^\pi |F(k)| dk, \quad (\text{S21})$$

$$\delta\zeta(t) = \frac{1}{2\pi} \int_0^\pi |F(k)| \cos(4|\mathbf{B}(k)|t) dk. \quad (\text{S22})$$

The $\zeta(\infty)$ means the stationary part of $\zeta(t)$ and $\delta\zeta(t)$ means the oscillatory part. After evaluating through the saddle point integration in the continuum limit, we will find that $\delta\zeta(t)$ behaves as a damping oscillation and that the

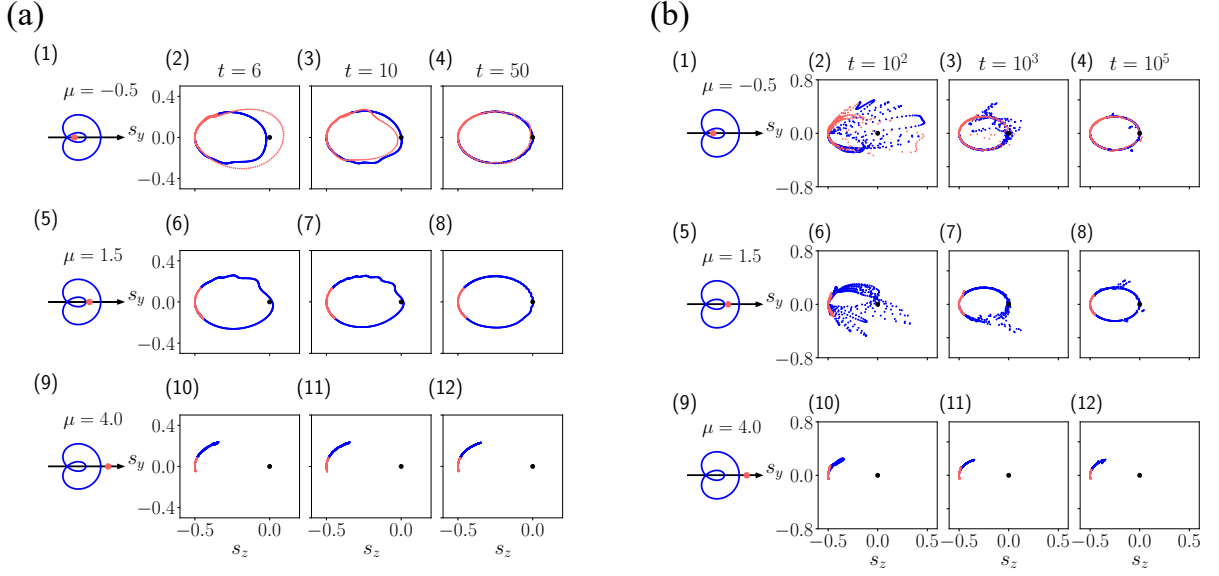


FIG. S2. Plots of (a) time-averaged $\{\bar{r}_\alpha^t(k, t)\}$ and (b) momentum-averaged $\{\bar{r}_\alpha^k(k, t)\}$ at different times. The left panel of each subfigure illustrates the considered system. To indicate the ranges, blue dots represent $[0, \pi)$ and red dots represent $[\pi, 2\pi)$. Other parameters are set as follows: $N = 10^6$, $\Delta k = \frac{\pi}{10^3}$, $\kappa_1 = 1$, $\kappa_2 = 2$, $\Delta_1 = 1$, and $\Delta_2 = 1$.

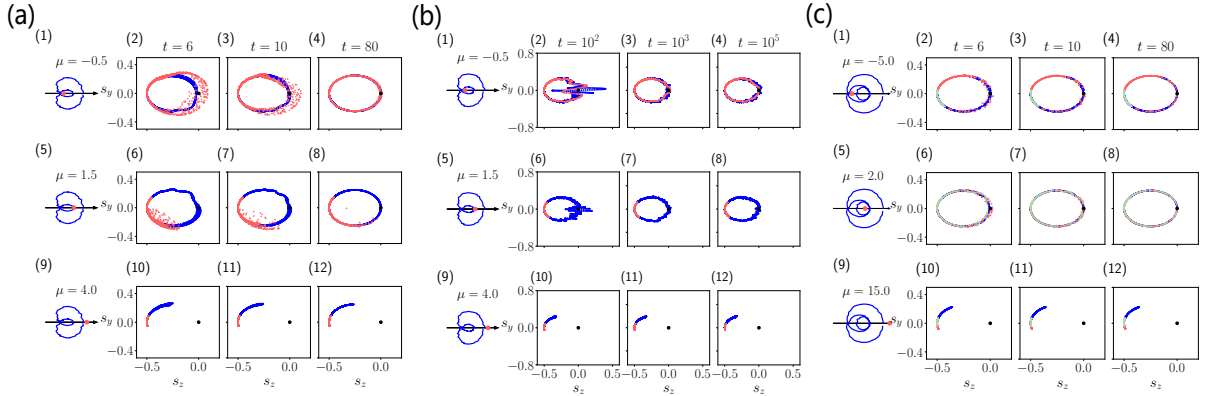


FIG. S3. Plots of (a) time-averaged $\{\bar{r}_\alpha^t(k, t)\}$ and (b) momentum-averaged $\{\bar{r}_\alpha^k(k, t)\}$ at different times for the non-uniform μ . The left panel of each subfigure illustrates the considered system. To indicate the ranges, blue dots represent $[0, \pi)$ and red dots represent $[\pi, 2\pi)$. Other parameters are set as follows: $N = 10^6$, $\Delta k = \frac{\pi}{10^3}$, $\kappa_1 = 1$, $\kappa_2 = 2$, $\Delta_1 = 1$, $\Delta_2 = 1$, and $\delta = 0.5$. (c) $\{\bar{r}_\alpha^t(k, t)\}$ for the extended Kitaev chain. To indicate the ranges, blue dots represent $[0, 2\pi/3)$, red dots represent $[2\pi/3, 4\pi/3)$ and cyan dots represent $[4\pi/3, 2\pi)$. Other parameters are set as follows: $\kappa_1 = 1$, $\kappa_2 = 4$, $\kappa_3 = 6$, $\Delta_1 = 1$, $\Delta_2 = 2$, $\Delta_3 = 3$, and $\delta = 0.5$.

decay rate depends on the location k_0 of the extrema $|\mathbf{B}(k)|$. (i) In the case where $k_0 \neq 0, \pi$, the quasi frequency is approximately $\omega \approx 2|\mathbf{B}(k_0)|$, and the decay of $\delta\zeta(t)$ follows a power law with $\sim t^{-0.5}$. (ii) In the case where $k_0 = 0, \pi$, the quasi frequency is approximately $\omega \approx 2|\mathbf{B}(k_0 = 0)|$, and the decay of $\delta\zeta(t)$ follows a power law with $\sim t^{-1}$. These findings are consistent with the plots presented in Fig. S5(a) and (b). In conclusion, we obtain

$$\bar{\zeta}(t \rightarrow \infty) = \zeta(t \rightarrow \infty). \quad (\text{S23})$$

This means that ζ could play the same role as $\bar{\zeta}$.

In the following, we focus on the analytic form of $\bar{\zeta}$. Although the explicit form has been provided in Ref. [3], we

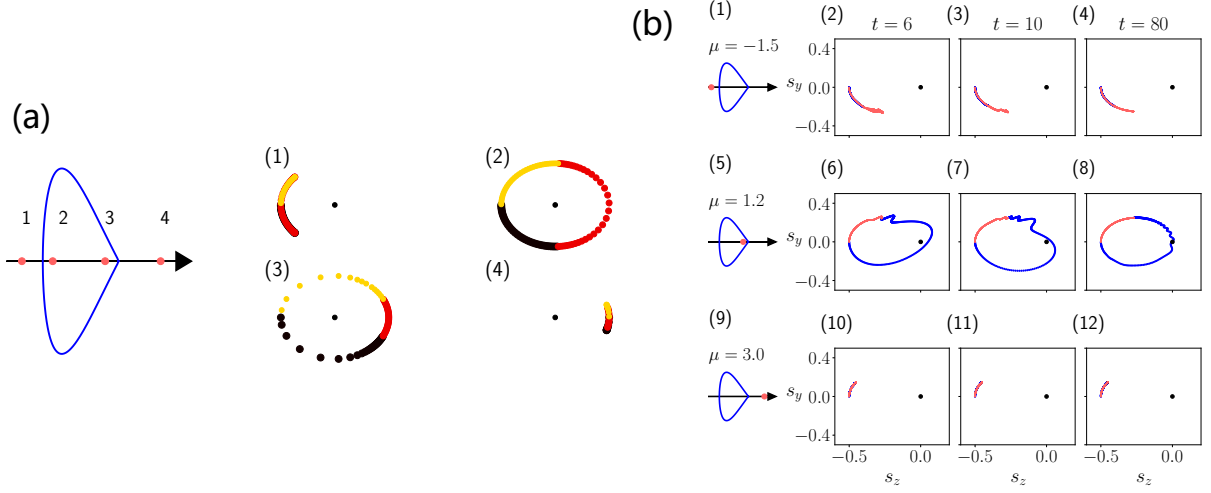


FIG. S4. The description of topological property for the inverse-square decay. (a) Geometric representation for the topological property in the parametric space. The left panel illustrates the curve of the magnetic field, $\mathbf{B}(k)$. The red dots represent the origin of the parametric space, $\mu = -1.5, -0.5, 1.2,$ and 3 , which determine the topology of the Hamiltonian. The right panel shows the curves of the pseudo-spin vector of the GS. (b) Time-averaged pseudo-spin $\{\bar{\mathbf{r}}_{\alpha}^t(k, t)\}$.

establish the conclusion from the perspective of pseudo-spin vectors here. We rewrite the form of $F(k)$,

$$F(k) = \frac{1}{2} \sin 2\vartheta_k, \quad (\text{S24})$$

with $\vartheta_k = \sin^{-1} \left[\frac{\bar{r}_y(k)}{|\bar{\mathbf{r}}(k)|} \right]$ and then

$$\bar{\zeta} = \frac{1}{4\pi} \int_0^{\pi} |\sin 2\vartheta_k| dk. \quad (\text{S25})$$

Here we introduce a new angle φ_k , which is equal to ϑ_k when $\Delta = 1$,

$$\sin \varphi_k = \frac{\bar{r}_y(k, \Delta = 1)}{|\bar{\mathbf{r}}(k, \Delta = 1)|}. \quad (\text{S26})$$

It can be easily proven that the relations between φ_k and k are

$$|\mathbf{B}(k, \Delta = 1)| \sin \varphi_k = \sin k, \quad (\text{S27})$$

$$|\mathbf{B}(k, \Delta = 1)| \cos \varphi_k = \cos k - \mu. \quad (\text{S28})$$

Furthermore, we can establish the relation between φ_k and ϑ_k

$$\tan \vartheta_k = \Delta \tan \varphi_k. \quad (\text{S29})$$

Based on the relations in Eqs. (S27) and (S28), we can express dk by $d\varphi_k$ and then substitute the result into Eq. (S24). Thus, we obtain,

$$\bar{\zeta} = \frac{1}{4\pi} \int_0^{\Theta} \frac{|\sin 2\vartheta_k| |\mathbf{B}(k, \Delta = 1)|}{\cos(k - \varphi_k)} d\varphi_k. \quad (\text{S30})$$

Now let us consider the contributions of the pair of pseudo-spin vectors $\bar{\mathbf{r}}(k_1)$ and $\bar{\mathbf{r}}(k_2)$ with the same value of $\sin \vartheta_k$. In the nontrivial region, as shown in Fig. S5(c), we have

$$\vartheta_{k_1} = \pi - \vartheta_{k_2}. \quad (\text{S31})$$

In the trivial region, as shown in Fig. S5(d), we have

$$\vartheta_{k_1} = \vartheta_{k_2}. \quad (\text{S32})$$

It is easy to observe that regardless of whether the region is trivial or nontrivial, we obtain the following relation,

$$\frac{|\mathbf{B}(k_1, \Delta = 1)|}{\cos(k_1 - \varphi_{k_1})} + \frac{|\mathbf{B}(k_2, \Delta = 1)|}{\cos(k_2 - \varphi_{k_2})} = 2. \quad (\text{S33})$$

Thus, the value of $\bar{\zeta}(\infty)$ can be expressed as

$$\bar{\zeta} = \frac{1}{2\pi} \int_0^\Theta |\sin 2\vartheta_k| d\varphi_k. \quad (\text{S34})$$

Again the initial state, $|\psi(0)\rangle = \prod_l^N |0\rangle_N$, represents the GS of the pre-quenched topological trivial Hamiltonian in the coordinate space when $\mu \rightarrow \infty$. It is evident that when the post-quenched Hamiltonian resides in the nontrivial region, the upper limit $\Theta = \pi/2$, allowing $\zeta(\infty)$ to attain a value independent of μ . However, in the case of the post-quenched Hamiltonian being in the topologically trivial region, $\Theta = \arcsin \frac{1}{\mu}$. One can readily observe the nonanalytic behavior of $\bar{\zeta}$ when the system crosses the boundary.

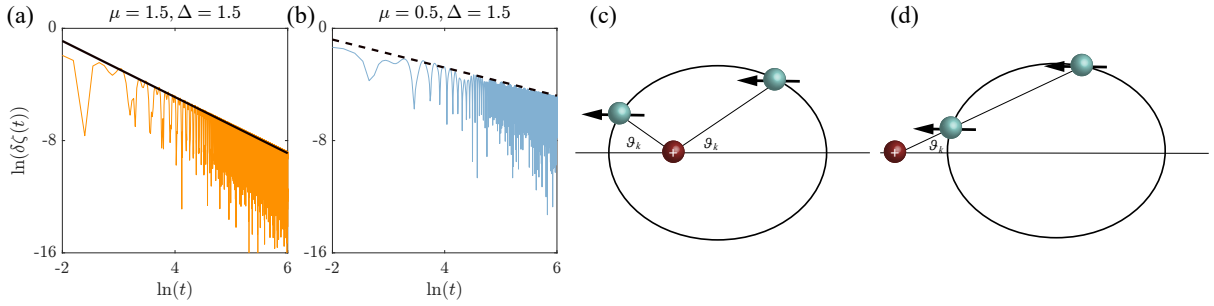


FIG. S5. Plots of $\ln(\delta\zeta(t))$ as a function of $\ln(t)$. In (a) we set $\mu = 1.5$ and $\Delta = 0.5$ and the location of extrema $|\mathbf{B}(k)|$ is $k_0 = 0$. While in (b) $\mu = 0.5$ and $\Delta = 0.5$ and the location is $k_0 = 0.84$. The slopes of the solid black and dashed black lines in (a) and (b) are -1 and -0.5 , respectively. These results correspond with our analysis of the power law of $\delta\zeta(t)$. (c)-(d) sketched the pair of the pseudo spins, which serves as the building block for understanding the emergence of the plateau in Fig. 3(b) of the main text.

* zhangxz@tjnu.edu.cn

† songtc@nankai.edu.cn

- [1] T. Suzuki, T. Someya, T. Hashimoto, S. Michimae, M. Watanabe, M. Fujisawa, T. Kanai, N. Ishii, J. Itatani, S. Kasahara, *et al.*, *Communications Physics* **2**, 115 (2019).
 [2] G. Zhang, C. Li, and Z. Song, *Scientific Reports* **7**, 8176 (2017).
 [3] Y. Shi, K. Zhang, and Z. Song, *Physical Review B* **106**, 184505 (2022).